

1 **Characteristics of airborne black carbon-containing particles**
2 **during the 2021 summer COVID-19 lockdown in a typical**
3 **Yangtze River Delta city, China**

4
5 Yuan Dai^{1,2,3}, Junfeng Wang^{1,2}, Houjun Wang³, Shijie Cui^{1,2}, Yunjiang Zhang^{1,2},
6 Haiwei Li^{1,2}, Yun Wu^{1,2}, Ming Wang^{1,2}, Eleonora Aruffo⁵, Xinlei Ge^{1,2,4*}

7
8 ¹Jiangsu Key Laboratory of Atmospheric Environment Monitoring and Pollution
9 Control, Collaborative Innovation Center of Atmospheric Environment and Equipment
10 Technology, School of Environmental Science and Engineering, Nanjing University of
11 Information Science and Technology, Nanjing 210044, China

12 ²International Joint Laboratory on Climate and Environment Change (ILCEC), Nanjing
13 University of Information Science and Technology, 210044 Nanjing, China

14 ³Yangzhou Environmental Monitoring Center, Yangzhou 225009, China

15 ⁴School of Environment and Energy Engineering, Anhui Jianzhu University, Hefei
16 230601, China

17 ⁵Department of Advanced Technologies in Medicine & Dentistry, University “G.
18 d’Annunzio” of Chieti-Pescara; Center for Advanced Studies and Technology-CAST,
19 Chieti 66100, Italy

20
21 **Correspondence:** Xinlei Ge (caxinra@163.com)

样式定义: 普通(网站)

设置了格式: 字体颜色: 自动设置

设置了格式: 字体颜色: 自动设置

22 **Abstract**

23 Black carbon-containing particles (BCc) are ubiquitous in ambient air, significantly
24 contributing to particulate matter (PM) pollution. The unexpected outbreak of the
25 COVID-19 pandemic in the summer of 2021 prompted a localized and prolonged
26 lockdown in Yangzhou City, situated in the Yangtze River Delta, China. This lockdown
27 led to significantly altering in local anthropogenic emissions, while neighboring cities
28 continued regular operations, providing a unique opportunity for the investigation of
29 BCc characteristics influenced by varying emission conditions. Single particle aerosol
30 mass spectrometer (SPA-MS) analysis revealed a notable decrease in the proportion of
31 freshly emitted BCc during the lockdown period (LD). However, ~~we did observe a~~
32 ~~concurrent 7%PM_{2.5} concentrations remained relatively unchanged, with an observed~~
33 ~~increase in PM_{2.5} concentration during LD, with a higher the~~ proportion of aged BCc
34 ~~during LD~~ compared to the period before the lockdown (BLD). ~~Evidence shows that~~
35 ~~The study also underscored the significant role of~~ regional ~~transportation plays a vital~~
36 ~~role-transport in the enhancement of~~PM_{2.5} ~~pollution during LD~~the campaign. Moreover,
37 reactive trace gases (e.g., NO_x, SO₂, and VOCs) could form thick coatings on pre-
38 existing particles likely via enhanced heterogeneous hydrolysis under high ~~relative~~
39 ~~humidity (RH)~~ as well, resulting in significant BCc particle growth (~600 nm), as well
40 as PM_{2.5}, during LD. ~~Our study highlights that short-term, strict local emission controls~~
41 may not effectively reduce PM pollution due to the complex production and
42 transmission characteristics of BCc and the non-linear responses of PM_{2.5} to its
43 precursors. Achieving further effective PM_{2.5} reduction mandates a focus on nuanced
44 control of BCc and necessitates a comprehensive and extensive approach with a
45 regionally coordinated and balanced control strategy through joint regulation.

设置了格式: 非突出显示

46 **1. Introduction**

47 China has implemented long-term clean air measures to cut down anthropogenic
48 emissions and improve air quality (Ge et al., 2020), resulting in a nationwide reduction
49 of average fine particulate matter (PM_{2.5}, aerodynamic diameter ≤ 2.5 μm) level from
50 50 μg m⁻³ in 2015 to 30 μg m⁻³ in 2020 (Zhou et al., 2022). However, this PM_{2.5}
51 concentration remains significantly higher than the new World Health Organization
52 (WHO) guideline value of 5 μg m⁻³ (WHO Global Air Quality Guidelines, 2021).

53
54 Black carbon (BC) is a ubiquitous component of aerosols, typically constituting a small
55 proportion (5~10%) of PM_{2.5} in the atmosphere (Chen et al., 2020). However, freshly
56 emitted BC evolves into BC-containing particles (BCc) by undergoing atmospheric
57 aging, contributing to a rise in the total mass of PM_{2.5} through processes of coating or
58 embedding by other materials (Bond and Bergstrom, 2006; Peng et al., 2016). The
59 number and mass fraction of BCc can exceed 60% and 50% of PM_{2.5}, respectively,
60 emphasizing the significant role of BC in elevating the mass concentration of
61 particulate matter (PM) (Sun et al., 2022; Xie et al., 2020; Chen et al., 2020).

62
63 The atmospheric aging of BCc involves intricate chemical and physical transformations
64 that influence their mixing state, morphology, hygroscopicity, and optical properties,
65 all of which have profound implications for climate and human health (Bond et al.,
66 2013; Ramanathan et al., 2008). For example, freshly emitted BC particles are initially
67 hydrophobic but possess a porous surface structure that facilitates the internal or
68 external mixing with co-emitted primary organic/inorganic and secondary materials
69 that are associated with BC (Cheng et al., 2012; Li et al., 2020). On the other hand, BCc
70 undergoes continually aging processes, including the condensation of low-volatility
71 vapors (Li et al., 2022), coagulation with preexisting aerosols (Kondo et al., 2011), and
72 heterogeneous oxidation with gaseous pollutants (Zhang et al., 2024). This alteration
73 may affect the coating thickness, morphology, size distribution, and hygroscopicity of
74 BCc, thereby impacting their climate forcing as well as atmospheric lifetime (Luo et al.,
75 2022; Taylor et al., 2014). High loading of atmospheric BCc could also depress the
76 development of the planetary boundary layer and exacerbate PM pollution episodes
77 (Huang et al., 2018). BCc characteristics are influenced by various combustion sources
78 and emission conditions, including local industrial burning, vehicle exhausts,
79 residential coal burning, and biomass burning (Li et al., 2020; Sedlacek et al., 2022;
80 Zhang et al., 2018), as well as long-range transport from other regions (Adachi et al.,
81 2014; Zhang et al., 2021). Those diverse conditions complicate the development of
82 parameterizations of BCc properties, the insufficient understanding of complex
83 emission sources, aging processes, and physical properties of BCc, hampering the
84 effectiveness of air quality remediation (Cappa et al., 2019; Kahnert, 2010; Sun et al.,
85 2021).

86
87 Studies on the effects of large-scale and short-term stringent emission control events on

设置了格式: 字体: Times New Roman

设置了格式: 非突出显示

设置了格式: 非突出显示

设置了格式: 非突出显示

设置了格式: 非突出显示

设置了格式: 非突出显示

设置了格式: 非突出显示

设置了格式: 非突出显示

设置了格式: 非突出显示

设置了格式: 非突出显示

设置了格式: 非突出显示

设置了格式: 非突出显示

设置了格式: 非突出显示

设置了格式: 非突出显示

设置了格式: 非突出显示

设置了格式: 非突出显示

设置了格式: 非突出显示

设置了格式: 非突出显示

设置了格式: 非突出显示

设置了格式: 非突出显示

设置了格式: 非突出显示

域代码已更改

88 air quality in China have been widely deployed, e.g., the 2008 Beijing Olympic Games
89 (Wang et al., 2010; Zhou et al., 2010), the 2015 Asia-Pacific Economic Cooperation
90 (APEC) (Zhu et al., 2015), the 2014 Nanjing Youth Olympic Games (Wang et al., 2022)
91 and the national COVID-19 lockdown in 2020 winter (Huang et al., 2021; Le et al.,
92 2020; L. Li et al., 2020; Wang et al., 2020). Previous studies extensively investigated
93 air pollutant variations during the COVID-19 lockdown in the winter of 2020 across
94 different regions of the world. Stringent restrictions on industrial and vehicular
95 activities have resulted in significant reductions in gaseous pollutants and particulate
96 matter, not only in megacities (Chen et al., 2020; Jeong et al., 2022; Sun et al., 2020)
97 but also in middle-sized cities (Clemente et al., 2022; Wang et al., 2021; Xu et al., 2020)
98 and rural areas (Cui et al., 2021, 2020; Jain et al., 2021). Compared to the decreasing
99 trends observed in most cities worldwide, the level of PM_{2.5} in Shanghai (Chang et al.,
100 2020), Hohhot (Zhou et al., 2022), and the Northeast of China Plain (Nie et al., 2021)
101 increased unexpectedly. These observations reveal the complex aerosol chemistry of
102 PM_{2.5} comprising primary and secondary components. The reduction of primary
103 pollutants during lockdown resulted in a shift towards a higher proportion of secondary
104 aerosols, including inorganic and organic species, exhibiting a non-linear response to
105 emission changes (Zhang et al., 2021). Furthermore, some studies suggested that the
106 increase in secondary aerosols during lockdown is due to the enhanced atmospheric
107 oxidative capacity resulting from the rise in ozone levels (Wang et al., 2021),
108 unfavorable meteorological conditions (Chien et al., 2022; Sulaymon et al., 2021a),
109 changes of local and regional emission sources (Feng et al., 2022). However, most
110 previous studies focused on lockdown events during the cold seasons, and studies on
111 summer lockdown events in China were very limited.

112
113 Yangzhou is located in the central region of the Yangtze River Delta (YRD), at the
114 junction of the Yangtze River and, the Beijing-Hangzhou Grand Canal, which serves as
115 a prominent economic city, industrial-intensive area, and highly active inland shipping
116 node in East China. Due to the complex emissions and feedback with the East Asian
117 monsoons (Ding et al., 2019), this region is susceptible to anthropogenic aerosols,
118 especially BC_c originating from chemical, steelmaking, coal-fired, petrochemical
119 enterprises, and transportation, etc. Extensive studies have investigated the responses
120 of atmospheric pollutants to emission changes during the COVID-19 lockdown
121 measures in the YRD (Chen et al., 2021; Li et al., 2020; Qin et al., 2021; Zhang
122 et al., 2022). However, the key chemical and physical processes specifically responsible
123 for the BC_c in this region are still unclear. During the summer of 2021, Yangzhou
124 experienced a resurgence of COVID-19 with over 500 confirmed cases. In response,
125 stringent public health measures were imposed from July 28th to September 10th,
126 including the closure of public transport, and suspension of non-essential industrial
127 plants, restaurants, shopping malls, and entertainment clubs. People were also
128 mandated to quarantine at home. Consequently, Yangzhou experienced a significant
129 decline in transportation and industrial energy consumption, dropping by nearly 46%

130 [and 25%, respectively, compared to the same period in 2020 \(www.yangzhou.gov.cn\)](http://www.yangzhou.gov.cn),
131 [implying a substantial reduction in human activity and primary emissions](#). Unlike the
132 nationwide COVID-19 lockdown in China during the cold season of 2020 (Le et al.,
133 2020; Sulaymon et al., 2021b), the summer lockdown in Yangzhou was more localized
134 but protracted, significantly altering local anthropogenic emissions while neighboring
135 cities maintained regular operations, which provides a unique opportunity to explore
136 and compare the diverse mixing states and, the aging process of BCc in different
137 anthropogenic emission conditions in summer.

138
139 Here we report the chemical compositions and aging characteristics of airborne BCc in
140 YRD. Our investigation involved a combination of ground measurements, spaceborne
141 observations, and mass spectrometric analysis conducted during the COVID-19
142 lockdown in the summer of 2021 in Yangzhou. Additionally, we employed potential
143 source contribution function (PSCF) analysis to investigate the air pollution patterns in
144 the YRD.

145 146 **2. Methods**

147 **2.1 Sampling site and instruments**

148 The in-situ online measurements were conducted at a rooftop laboratory 20 m above
149 ground located in a national air quality monitoring station, Yangzhou Environmental
150 Monitoring Center (32.41°N, 119.40°E), Yangzhou, China (~~Figure 1~~;~~Figure 1~~). This
151 sampling site is a typical urban site surrounded by residential areas, arterial roads, parks,
152 restaurants, and shopping centers. In this study, the measurement period was divided
153 into three phases: the before-lockdown period (BLD: 30 June to ~~27~~²⁸ July 2021), the
154 lockdown period (LD: ~~28~~²⁹ July to 9 September 2021), and the after-lockdown period
155 (ALD: 10 September to 7 October 2021) (~~Figure 2~~;~~Figure 2~~).

156
157 A single-particle aerosol mass spectrometer (SPA-MS, Hexin Analytical Instrument Co.,
158 Ltd., China) was deployed during the field campaign to obtain the chemical
159 composition, size distribution, and mixing state of individual PM_{2.5} particles. A cyclone
160 with a 2.5 μm cutpoint (Model URG-2000-30ED) and a Nafion dryer is equipped in
161 front of the sampling inlet. Individual particles are introduced into the SPA-MS through
162 a critical orifice at a flow rate of 3 L min⁻¹. The vacuum aerodynamic diameters (D_{va})
163 are determined using the velocities derived from two continuous laser beams (diode Nd:
164 YAG, 532 nm) spaced 6 cm apart. Subsequently, these particles are desorbed and
165 ionized by a downstream pulsed laser (266 nm), and ion fragments are generated and
166 measured by a Z-shaped bipolar time-of-flight mass spectrometer. A more detailed
167 description of SPA-MS can be found in previous studies (Li et al., 2011).

168
169 PM_{2.5} mass concentration was measured by a particulate matter monitor (XHPM2000E,
170 Xianhe, China). Nitrogen oxides (NO_x = NO + NO₂), SO₂, and ozone (O₃)
171 concentrations were detected with a set of Thermo Fisher Scientific instruments

设置了格式: 字体: Times New Roman

172 (Models 42i, 43i, and 49i). The concentrations of 103 volatile organic compounds
173 (VOCs) in ambient air, comprising 57 ozone precursors (PAMS), 12 aldehydes and
174 ketones, and 34 toxic organics (TO15), were continuously monitored at hourly intervals
175 using an online device (TH-300B, Tianhong, China). Meteorological parameters,
176 including ambient temperature (T), relative humidity (RH), ~~precipitation (PCP)~~, wind
177 direction (WD), and wind speed (WS) were observed synchronously using an automatic
178 weather instrument (WXT530, Vaisala, Finland). Precipitation (PCP) data was obtained
179 from the Yangzhou Meteorological Bureau. All online data presented in this paper were
180 hourly averaged at local time (Beijing time, UTC+8).

182 2.2 Data analysis

183 2.2.1 Satellite Product

184 In this study, we utilized the Copernicus Atmosphere Monitoring Service (CAMS)
185 Global Near-Real-Time dataset (available at <https://developers.google.com/earth->
186 [engine/datasets/catalog/ECMWF_CAMS_NRT](https://developers.google.com/earth-engine/datasets/catalog/ECMWF_CAMS_NRT)), acquired from the European Centre
187 for Medium-Range Weather Forecasts (ECMWF), to analyze the distribution of total
188 surface column concentrations of NO₂, SO₂ and surface PM_{2.5} mass concentration.
189 CAMS offers the capacity to continuously monitor the composition of the Earth's
190 atmosphere at global and regional scales since 2016, with a spatial resolution of 44528
191 meters (Benedetti et al., 2009; Morcrette et al., 2009). The details of the bands of the
192 dataset used in this study are shown in Table S2. We calculated and plotted the averaged
193 2-dimensional data of ECMWF/CAMS/NRT NO₂, SO₂, and PM_{2.5} during BLD and LD
194 over the region of interest (17.93~54.74 °N, 71.21~142.23 °E) using Google Earth
195 Engine (Gorelick et al., 2017). The integration of remote sensing measurements has
196 provided a more comprehensive understanding of the sources and distributions of
197 particle matter and gaseous pollutants facilitating the evaluation of the impact of human
198 activities on air quality.

199 2.2.2 Geographic Source Analysis

200 The potential source contribution function (PSCF) analysis, based on the Hybrid
201 Single-Particle Lagrangian Integrated Trajectory (HYSPPLIT) model, can be employed
202 to identify regional sources of air pollutants. Before conducting the PSCF analysis, 36
203 hours of air mass backward trajectories with one-hour resolution at 500 m above ground
204 level were calculated using the wind data from the Global Data Assimilation System
205 (GDAS) provided by the National Oceanic and Atmospheric Administration (NOAA)
206 (Wang et al., 2009). An open-source software MeteoInfo (Wang, 2014) was utilized for
207 the PSCF analysis. The whole study area (110.1~133.4 °E and 21.3~39.9 °N) covered
208 by the trajectories was divided into thousands of cells with a spatial resolution of 0.1°
209 × 0.1°. The PSCF was simulated according to the following equation:

$$210 \quad PSCF_{ij} = \frac{m_{ij}}{n_{ij}} \quad (1)$$

211 where $PSCF_{ij}$ is the conditional probability that the grid cell (i, j) was a source of the

设置了格式: 字体: Times New Roman

设置了格式: 非突出显示

设置了格式: 非突出显示

设置了格式: 非突出显示

设置了格式: 非突出显示

设置了格式: 非突出显示

212 species found in high concentration (Hopke et al., 1993); n_{ij} is the number of all
 213 trajectories passing through this grid cell, and m_{ij} is the number of trajectories. In this
 214 study, the pollution criterion values for different BCc particle types were set as the 75th
 215 percentile of hourly average number fractions, respectively. To further improve the
 216 accuracy of the PSCF analysis and minimize analytical uncertainties, the Weighted
 217 PSCF (WPSCF) functions as shown in Equation (2~3) were applied (Polissar et al.,
 218 1999). The weight (W_{ij}) for each grid cell was determined based on the number of
 219 trajectory endpoints (n_{ij}) as follows:

$$220 \quad WPSCF_{ij} = W_{ij} \times PSCF_{ij} \quad (2)$$

$$221 \quad W_{ij} = \begin{cases} 1.00 & n_{ij} > 3n_{ave} \\ 0.70 & 1.5n_{ave} < n_{ij} \leq 3n_{ave} \\ 0.40 & n_{ave} < n_{ij} \leq 1.5n_{ave} \\ 0.17 & n_{ij} \leq n_{ave} \end{cases} \quad (3)$$

222 Here, n_{ave} is the average number of trajectory endpoints of each grid.

223 2.2.3 SPA-MS Data Analysis

224 In total, 1649574 particles were analyzed during the entire observation period. The size
 225 and chemical composition of single particles were analyzed using the Computational
 226 Continuation Core (COCO V1.4) toolkit in MATLAB 2022 (The MathWorks, Inc.).
 227 Our focus was on BCc, which was identified based on the relative peak area (RPA) of
 228 carbon ion clusters (C_n^+ , $n = 1, 2, 3, \dots$), with a threshold of 0.05 (Zhang et al., 2021).
 229 An adaptive resonance theory-based neural network algorithm (ART-2a) was applied
 230 to classify the measured individual particles based on the presence and intensity of ion
 231 peaks, with a vigilance factor of 0.75, a learning rate of 0.05, and 20 iterations (Song et
 232 al., 1999).

234 3. Results and discussion

235 3.1 Field observations

236 **Figure 2** presents the temporal variations of meteorological parameters, $PM_{2.5}$,
 237 NO_x , and SO_2 concentrations. Notably, significantly reductions in $PM_{2.5}$, NO_x , and SO_2
 238 were significantly reduced/observed at the end of BLD due to a high precipitation event,
 239 with a peak hourly precipitation reaching 37 mm, and the data collected during ~~the~~
 240 ~~precipitation-this event~~ were excluded from the ~~data~~-analysis. During BLD, the mean
 241 temperature (T) was 28 ± 3 °C, the total precipitation was 221 mm, with an average
 242 relative humidity (RH) of ~~81 ± 11~~ 83 ± 12%. The prevailing winds originated from the
 243 south and southeast, with a mean wind speed (WS) of ~~3.4 ± 0.9~~ 3 ± 1.2 m s⁻¹. In
 244 comparison, LD shows a decline in temperature to ~~26.27 ± 2~~ 26 ± 2 °C and WS to ~~2.3 ± 1.0-8~~ 2.3 ± 1.0-8 m
 245 s⁻¹, but an increase in RH to ~~87 ± 10%~~ 87 ± 11% and a reduction in total precipitation to 86
 246 mm. **Figure S2b and c** present uniform distributions of RH and boundary-layer height
 247 (BLH) across the YRD during LD. ~~The implication is that the resemblance of these~~
 248 regional meteorological conditions ~~in YRD and~~ the effective removal of the pollutants

设置了格式: 字体: Times New Roman

249 accumulated at the end of BLD, ~~provides a favorable condition for investigating the~~
250 ~~facilitated the investigation of BCs~~ regional transport of BCs during LD in
251 Yangzhou YRD. During ALD, the temperature declined further to 25 ± 3 °C, the WS
252 increased to 3.23 ± 1.45 m s⁻¹, and RH ~~decreased~~ total precipitation dropped to 27 mm
253 with a lower level RH of 75 ± 15 to 77 ± 14 %.

254
255 ~~Surface During LD, strict measures resulted in notably lower surface~~ concentrations of
256 ~~PM_{2.5} (20.3 μg m⁻³), NO_x (4916.8 μg m⁻³) and TVOC (5655.9 μg m⁻³) were the lowest~~
257 ~~during LD~~ compared to those of BLD and ALD, whereas, Conversely, the surface O₃
258 concentration showed an increase of 1318.4 μg m⁻³ (19%) during LD
259 ~~compared relative~~ to BLD. The reduction of fresh NO emission alleviates O₃ titration
260 (Steinfeld, 1998) could be an explanation. Furthermore, analysis from Figure
261 S3 indicates that the O₃ level is higher than those of neighboring cities in the YRD,
262 suggesting higher local atmospheric oxidation capacity during LD. However, the
263 average concentrations of PM_{2.5} (19.9 vs. 21.2 μg m⁻³), SO₂ (9.41 vs. 9.52
264 μg m⁻³) and CO (0.61 vs. 0.64 mg m⁻³), and TVOC (58 vs. 56 μg m⁻³), were
265 comparable during both BLD and LD (Figure 3).

266
267 After LD, social activities gradually resumed in Yangzhou City, leading to an apparent
268 increase in all observed pollutants during the ALD period. For instance, there were
269 relative increases of 7466% for NO_x, 2219% for SO₂, 5536% for TVOC, 3014% for O₃,
270 2932% for PM_{2.5}, and 1716% for CO from LD to ALD, respectively (Figure 3).
271 Given that both BC and CO are byproducts of incomplete combustion of carbon-
272 containing fuels (Wang et al., 2015), and the high correlation between BC and CO
273 (Zhou et al., 2009), it is plausible to infer that the primary emission source of BC during
274 LD was different with that differed from those during ALD. This change likely reflects
275 the shift in combustion practices and fuel usage patterns as economic activities restarted
276 during ALD.

277
278 Satellite-retrieved PM_{2.5}, NO₂, and SO₂ data over the entire region of eastern China
279 were also investigated, and results show that these pollutants were predominantly
280 concentrated in Shanghai and its neighboring cities, including Yangzhou, during both
281 BLD and LD (Figure S4). Figure 4 presents regional fractional changes,
282 including Yangzhou, of mean PM_{2.5}, NO₂, and SO₂ concentrations from the BLD to LD
283 periods in YRD, all showing an increase of 29%, 6%, and 14%, respectively. In
284 comparison, Yangzhou city experienced lower increases in these air pollutants, with
285 slight changes of 6.0%, -18.0%, and -4.3% for PM_{2.5}, NO₂, and SO₂, respectively. The
286 implication is that, even though local primary emissions, such as NO₂, and SO₂, were
287 reduced substantially during LD, they still could be affected by regional transport.
288 Furthermore, as depicted in Figure S3, the concentrations of NO₂ in major cities of the
289 YRD were more than twice higher than in Yangzhou during LD, confirming a relatively
290 lower local primary emissions due to the stringent lockdown. However, the higher level

- 设置了格式: 非突出显示
- 设置了格式: 非突出显示
- 设置了格式: 非突出显示
- 设置了格式: 非突出显示
- 设置了格式: 非突出显示
- 设置了格式: 非突出显示
- 设置了格式: 非突出显示
- 设置了格式: 非突出显示
- 设置了格式: 字体颜色: 红色, 非突出显示
- 设置了格式: 非突出显示
- 设置了格式: 非突出显示
- 设置了格式: 非突出显示
- 设置了格式: 非突出显示
- 设置了格式: 非突出显示
- 设置了格式: 非突出显示
- 设置了格式: 非突出显示
- 设置了格式: 字体颜色: 红色, 非突出显示
- 设置了格式: 非突出显示
- 设置了格式: 非突出显示
- 设置了格式: 字体颜色: 自动设置

291 of SO₂ in Yangzhou during LD may be attributed to the nearby power stations along the
292 Yangtze River, which were not impacted by the lockdown measures.

293 294 3.2 Chemical composition and size distribution of individual BCc

295 Based on the SPA-MS analysis, a total of 1068362 BCc was collected during the whole
296 study period. The BCc accounted for 59%, 69%, and 57% of the total number of
297 measured particles in the BLD, LD, and ALD periods, respectively. **Figure 5**
298 shows the normalized average mass spectra of BCc during three periods. Ion height in
299 each spectrum reflects the number fraction of the detected BCc with the corresponding
300 ion to the total BCc, while colors represent peak area ranges of detected ions. BCc in
301 BLD, LD, and ALD shown similar mass spectra at $m/z < 100$, with common peaks
302 including carbon ion clusters (C_n^+ , $n = 1\sim 7$), m/z 27[C₂H₃]⁺, 37[C₃H]⁺, 43[C₂H₃O]⁺,
303 51[C₄H₃]⁺, 63[C₃H₃]⁺, 46[NO₂]⁻, 62[NO₃]⁻, and 97[HSO₄]⁻. However, the abundance
304 of large m/z carbon ions (C_n^+ , $n > 7$) in both BLD and ALD periods was 1.5 times higher
305 than that in the LD. Previous studies have indicated that high-mass carbon ions may be
306 linked to traffic emissions, particularly those from diesel trucks (Xie et al., 2020; Liu et
307 al., 2019), and the observed reduction in such ions during LD suggests a decrease in
308 local vehicle emissions. This trend is also consistent with the changes observed in
309 aromatic compounds, e.g. m/z 119[C₉H₁₁]⁺.

310
311 Further, BCc was classified into 12 types based on the differences in chemical features
312 and temporal variations, as shown in **Table S1**. Fresh BC particles (BC-fresh) are those
313 freshly emitted without undergoing significant atmospheric processing (Ding et al.,
314 2021). Five types of BC-fresh particles were identified according to their ion markers:
315 (i) BC-pure is dominated by carbon clusters (C_n^+) with minor ion signals of inorganic
316 species, such as m/z 46[NO₂]⁻ and m/z 97[HSO₄]⁻ from nitrate and sulfate, respectively
317 (Xie et al., 2020); (ii) BCc from biomass burning (BB) are characterized by ion signals
318 at m/z 39[K]⁺, 45[CHO₂]⁻, 59[C₂H₃O₂]⁻, and 73[C₃H₅O₂]⁻, with a relative peak area
319 (RPA) more than 0.5 (Silva et al., 1999); (iii) coal combustion BCc (CC) typically
320 include small carbon clusters (C_n^+ , $n = 1\sim 4$), metal elements (e.g., m/z 7[Li]⁺, 23[Na]⁺,
321 27[Al]⁺, 56[Fe]⁺, 63[Cu]⁺ and 206/207/208[Pb]⁺), and organic carbon (38[C₃H₂]⁺,
322 43[C₂H₃O]⁺) peaks in the positive mass spectrum, while the strong signals of secondary
323 inorganic species (46[NO₂]⁻, 43[AlO]⁻, 62[NO₃]⁻, 80[SO₃]⁻, 97[HSO₄]⁻) in the
324 negative ion mode suggest that CC particles were long-distance transported or more
325 processed (Zhang et al., 2022; Zhang et al., 2009); (iv) particles from vehicle emission
326 (VE) are characterized by the presence of ion signals at m/z 40[Ca]⁺, 51[V]⁺, 55[Mn]⁺,
327 67[VO]⁺, 46[NO₂]⁻, 62[NO₃]⁻, and 79[PO₃]⁻, as well as high loadings of organic carbon
328 (41[C₃H₅]⁺, 43[C₂H₃O]⁺) and carbon clusters (C_n^+ , $n = 1\sim 4$) ion peaks (Yang et al., 2017);
329 (v) BCc that are internally mixed with more than one type (BB, CC, and VE) are
330 categorized as Mix type (Sun et al., 2022).

331
332 Aged BC particles, denote as BC-aged, undergo a series of chemical reactions and

设置了格式: 字体: Times New Roman

设置了格式: 非突出显示

设置了格式: 非突出显示

设置了格式: 非突出显示

333 physical transformations. These processes typically lead to changes in their morphology,
334 hygroscopicity, and optical properties as they are coated with other materials (He et al.,
335 2015). Six types of BCc are classified as BC-aged and are further grouped into BCOC
336 and BC-SNA, depending on whether they contain mainly organic carbon (OC) or
337 sulfate/nitrate/ammonium (SNA). First, BCOC types indicate BC-aged particles that
338 are internally mixed with OC. These particles are characterized by the presence of
339 carbon clusters (C_n^+) and $C_nH_m^+$ ions ($n = 1\sim6$, $m = 1\sim3$) in positive mass spectra (Xie
340 et al., 2020). On the other hand, BC-aged particles that do not mix with OC are named
341 BC-SNA indicating the mix with secondary inorganic species. Additionally, BCOC
342 particles with negative mass spectra dominated by nitrate ions ($46[NO_2]^-$ and $62[NO_3]^-$)
343 or sulfate ions ($97[H_2SO_4]^-$) are referred to as BCOC-N or BCOC-S, respectively;
344 otherwise, BCOC particles showing similar peak areas of nitrate and sulfate are named
345 BCOC-SN. The BC-SNA particles are further categorized as BC-N, BC-S, and BC-SN
346 based on similar principles. Note the remaining particles that cannot be classified into
347 either BC-fresh or BC-aged ones are denoted as BC-other. More details of BCc particle
348 types are shown in **Table S1** and **Figure S1** in the Supplement.

349
350 During BLD, the average number fraction of BC-fresh particles was 36% with sizes
351 mainly concentrated at 500 nm, similar to the mode size of BC-aged particles was 520
352 nm (~~Figure 6~~-(**Figure 6**)). The predominant BCc types during BLD were BCOC-S
353 and BC-S (24% and 12% by number), likely because sulfate was removed less
354 efficiently than organic matter (OM) and NO_3 by heavy precipitation, especially during
355 the warm seasons (Isokääntä et al., 2022). As shown in ~~Figures 6e~~**Figures 6c and d**,
356 the peak size of BC-SNA was larger than that of BCOC in all periods, indicating that
357 organics coated BCc generally had a relatively thin coating compared to those coated
358 by secondary inorganic species, which is consistent with previous studies (Sun et al.,
359 2016; Wang et al., 2019).

360
361 During the transition ~~effrom~~ BLD to LD, heavy ~~and continuous~~ precipitation occurred
362 from ~~the evening to~~ July 27th ~~and early morning of~~ 25th to July 28th (the eve of lockdown),
363 resulting in the removal of a majority of the pollutants ($PM_{2.5}$: $4 \mu g m^{-3}$, O_3 : $35 \mu g m^{-3}$,
364 NO_x : $8 \mu g m^{-3}$). ~~After that~~Following this environmental clearance, strict lockdown
365 measures were carried on and the implemented, resulting in a drastic reduction in
366 primary emissions were abruptly cut down. As a result, the number fraction of BC-fresh
367 particles significantly decreased from 37% to 28% and that of VE-type particles
368 dropped from 12% to 3% (by number). Expectedly, with the decrease in NO_x , an
369 obvious enhancement of O_3 was observed during LD (~~Figure 3~~-(**Figure 3**)). According
370 to previous studies (Huang et al., 2021; Laughner et al., 2021), large reduction of NO_x
371 may promote the formation of O_3 under a VOC-limited regime and enhance the
372 oxidation capacity of the local atmosphere, which may promote the number fraction of
373 BC-aged particles increased from 64% in the BLD to 72% in LD (~~Figure 7a~~(**Figure**
374 **7a**)), indicating the lockdown could accelerate aging of BCc through complicated

375 chemical reactions and/or physical coagulation. Additionally, the most abundant type
376 of BCc changed from BCOC-S (24% by number) in the BLD to BC-N (25%) in the LD
377 (Figure 7a)(Figure 7a), suggesting different BCc formation pathways. Despite the
378 abrupt reductions of NO_x (-39%) due to the city lockdown, it ~~should be aware~~
379 ~~is important to note~~ that the ~~PM_{2.5} concentration of PM_{2.5} only~~ slightly ~~increased~~
380 ~~decreased~~ during LD₇ (-1%), highlighting the non-linear relationship between primary emissions
381 and PM_{2.5} levels.

382
383 During ALD (PM_{2.5}: 26.7 μg m⁻³, NO_x: 2827.9 μg m⁻³, TVOC: 76.0 μg m⁻³), the number
384 fraction of BC-fresh particles rose from 28% (LD) to 31% (ALD), while the fraction of
385 VE particles also increased from 3% (LD) to 12% (ALD) (Figure 7a)(Figure 7a).
386 Notably, the size distributions of BC-fresh and BC-aged particles presented relatively
387 small peaks at 690 nm and 820 nm during ALD, in addition to the prominent peaks at
388 490 nm and 500 nm, which were different from those in the BLD and LD periods. These
389 small peaks were relatively close to the dominant sizes of BC-fresh and BC-aged
390 particles during LD (Figure 6)(Figure 6). This result suggests that a substantial
391 number of BCc with small sizes (around 500 nm) after the lockdown was lifted in
392 Yangzhou, owing to the sudden enhancement of primary emissions; on the other hand,
393 particles with large diameters (>690 nm) may have formed due to the participation of
394 more trace reactive gases (e.g., NO_x, SO₂, and VOCs) in continuous aging reactions,
395 resulting in thicker coatings on the surface of pre-existing particles and therefore a more
396 clear separation of two-mode sizes during the ALD period than during the other two
397 periods. This hypothesis was also supported by the increased number fraction of
398 BCOC-SN during the ALD period (Figure 7a)(Figure 7a). Similar findings have been
399 reported in the North China Plain (NCP) and the YRD during cold seasons, where
400 thicker coatings on secondary aerosols were also observed under lower RH (<70%)
401 (Zhang et al., 2021). This might be due to that particles with more organics and nitrate
402 can result in earlier deliquescence and provide aqueous surfaces that facilitate the
403 heterogeneous formation of secondary species under relatively low RH (Zhang et al.,
404 2021). Among the three periods, the difference between the mode sizes of BC-aged and
405 BC-fresh particles was the smallest (10 nm) during the ALD period (Figure 6a and
406 b)(Figure 6a and b). This size reduction can be attributed to the increased BCOC and
407 hydrophobic primary particles after lockdown (Figure 7)(Figure 7). Because the
408 internally mixed BCOC and hydrophobic primary particles may constrain further
409 growth of secondary BC-SNA particles (Liu et al., 2016; Zhang et al., 2018), thereby
410 leading to smaller-sized BC-aged particles. Moreover, the differences in BCc mode
411 sizes between ALD and BLD periods also reveal an interesting fact that the lockdown
412 effect may not only affect air quality during lockdown but also can influence the air
413 quality even after lockdown, as the resumed emissions after lockdown may be subjected
414 to different chemistry from that before lockdown.

415
416 Throughout the entire observation, the changes in the number fraction of BC-SNA

设置了格式: 字体: Times New Roman

设置了格式: 非突出显示

设置了格式: 非突出显示

设置了格式: 字体颜色: 自动设置

设置了格式: 字体颜色: 自动设置

设置了格式: 字体颜色: 自动设置

设置了格式: 字体颜色: 自动设置

设置了格式: 字体颜色: 自动设置

设置了格式: 字体颜色: 自动设置

设置了格式: 字体颜色: 自动设置

设置了格式: 字体颜色: 自动设置

设置了格式: 字体颜色: 自动设置

设置了格式: 字体颜色: 自动设置

设置了格式: 图案: 清除

设置了格式: 字体: Times New Roman

417 exhibited consistency with the variations in RH (Figure 7b), indicating that
418 BC tends to mix with ammonium sulfate and ammonium nitrate under high RH
419 conditions. Meanwhile, the number fraction of BCOC shows similar patterns as TVOC,
420 suggesting that high TVOC levels may facilitate the coating of organics on BC cores
421 under low RH condition. Figure 8 displays the number fraction of BCc species
422 as a function of $PM_{2.5}$. Overall, as $PM_{2.5}$ levels increased, the number fraction of BC-
423 aged particles also increased, while the proportion of BC-fresh particles decreased
424 during BLD and LD, indicating a clear transition from BC-fresh particles to more aged
425 ones, in line with the average size distribution during ALD has a small peak at 900 nm.
426 Specifically, the increase in $PM_{2.5}$ was driven by BCOC-S during BLD (Figure
427 8a), whereas BC-N played a vital role in the $PM_{2.5}$ increase during LD
428 (Figure 8b). Interestingly, the concentration of NO_x , the primary precursor
429 of BC-N, decreased by 31% and 41% during LD compared to BLD and ALD,
430 respectively (Figure 3), indicating a strong non-linear response of nitrate in
431 BCc to NO_x , likely due to much faster conversion of NO_x to nitrate upon enhanced
432 atmospheric oxidation capacity; additionally, the high proportion of BC-N during LD
433 might be attributed to regional transport, similar to that in Shanghai during 2020 winter
434 lockdown (Chang et al., 2020).

436 3.3 Chemical aging of BCc

437 As shown in Figure 5, in the average positive mass spectra of total BCc, the
438 peak areas of C_n^+ , OM, and metals contributed to more than 95% of the total, while
439 nitrate and sulfate peak areas accounted for more than 90% of the negative mass
440 spectral signal. To better elucidate the aging processes of BCc during different
441 lockdown periods, we summed the carbon clusters C_n^+ ($n = 1\sim 5$, accounting for more
442 than 99% of C_n) peak areas to represent BC, and the total peak area of sulfate, nitrate,
443 and ammonium (SNA) to represent the second inorganic components coated on BC.
444 Additionally, we defined the sum of positive peak areas, excluding C_n^+ and metals, as
445 OC to represent the OM coated on BC. These peak areas encompassed almost all the
446 coating materials, except for metals, of BCc. The changes in the mixing state and
447 morphology of BCc can provide insights into their aging characteristics, as reported
448 previously (Kandler et al., 2018; Moffet et al., 2013). In this study, we use OC/C_n and
449 SNA/C_n ratios to describe different types of chemical components coated on BC-fresh,
450 and we use the ratio of the mode size of BC-aged (D_{aged}) to that of contemporaneous
451 BC-fresh (D_{fresh}) to represent the aging degree of BCc.

452
453 Figure 9 illustrates the diurnal variations of the OC/C_n and SNA/C_n ratios
454 along with the size distribution of BCc during different periods. We observed that both
455 OC/C_n and SNA/C_n increased during nighttime and decreased during daytime. These
456 variations showed the prominent enhancements of nocturnal OM and SNA, which
457 could be attributed to the accelerated gas-to-particle partitioning and nocturnal
458 secondary formation of organic/inorganic components under high relative humidity

459 (RH > 85%) and relatively stagnant air mass ($WS < 3 \text{ m s}^{-1}$) (**Figure S5**). It is worth
460 noting that from BLD to LD and ALD, the intensity of diurnal variations of OC/C_n and
461 SNA/C_n increased obviously. This discrepancy can be attributed to several reasons. (i)
462 During BLD, the frequent precipitations effectively scavenged the particles (Isokääntä
463 et al., 2022); (ii) In contrast, stronger solar radiation and higher O₃ concentration during
464 LD promoted photochemical formations of OC and SNA; (iii) After lockdown, more
465 precursors due to increased local emissions may lead to more production of secondary
466 components than that during BLD as explained earlier. These results indicate that the
467 aging process and mixing state of BCc depend strongly on meteorological conditions
468 as well as emission sources in urban cities.

469
470 As shown in **Figure 9, Figure 9**, BCc with ~400 nm D_{va} exhibited significant diurnal
471 fluctuations in the OC/C_n and SNA/C_n ratios, during LD. There is a noticeable increase
472 in the proportion of BC-SNA particles during nighttime when RH is relatively high.
473 These observations suggest that nighttime heterogeneous hydrolysis may be considered
474 a key mechanism responsible for the formation of BCOC and BC-SNA particles.
475 According to Jacobson (2002), coagulation can be significant between particles with
476 sizes <100nm and >1μm but insignificant for particles of >300nm, when the total
477 particle number concentration is higher than 10⁴ cm⁻³. During LD, the OC/C_n and
478 SNA/C_n ratios of BCc with ~400 nm D_{va} exhibited pronounced diurnal variations
479 (**Figure 9, Figure 9**) and the number fraction of BC-SNA increased obviously. Despite
480 the difference between D_{va} and physical diameter, such results imply that chemical
481 reactions should be considered as the major pathway for BCOC and BC-SNA particles
482 of ~400 nm D_{va}, while the large-sized BC-aged particles (>1 μm) may be partially from
483 physical coagulation. Additionally, the larger mode peak (600 nm, D_{va}) and higher
484 D_{aged}/D_{fresh} ratios (1.11) were observed compared to those of BLD (510 nm, 1.03) and
485 ALD (500 nm, 1.02) (**Figure 6, Figure 6**). Since RH was significantly higher during
486 LD (average RH of 87%) than BLD (average RH of 81%) and ALD period (average
487 RH of 75%), this result again supports that aqueous or heterogeneous reactions might
488 play a more important role to facilitate the chemical conversion of trace reactive gases
489 (e.g., SO₂, NO_x, and VOCs) and then formed a thicker coating on the surfaces of BC
490 cores, leading to evident growth in the size of BCc. This aqueous or heterogeneous
491 process during LD likely converted partially coated particles to fully thickly coated BCc
492 as well.

493 494 3.4 Source apportionment of BCc during lockdown

495 In addition to local emissions, regional transport plays a significant role in influencing
496 pollutant levels. The emergent lockdown in Yangzhou led to strict limitation on local
497 emissions, while surrounding cities were still running as usual. This is supported by
498 **Figure S6**, which illustrates the PM_{2.5} concentrations in Yangzhou and the other five
499 surrounding YRD cities (e.g., Nanjing, Zhenjiang, Changzhou, Taizhou, and Chuzhou)
500 during the campaign. High correlations between PM_{2.5} concentrations in Yangzhou and

设置了格式: 字体: Times New Roman

501 the other five cities were observed across all different periods (**Figure S6**). These
502 findings underscore the importance of the regional transport in PM_{2.5} pollution during
503 the campaign, providing ~~ana~~ unique opportunity to investigate the transmission and
504 source characteristics of BCc in YRD during summer. Herein, PSCF analysis was
505 applied to qualitatively simulate the source probability distributions of the specific BCc
506 particle types (BC-fresh, BC-aged, BCOC, and BC-SNA) during LD.

507
508 As shown in ~~Figure 10, Figure 10~~, the hotspots of potential sources for the four particle
509 types exhibited strong agreements with each other and primarily concentrated in the
510 southeast of Yangzhou, especially along the coast of the Yangtze River, with the
511 WPSCF greater than 0.6. These hotspot areas also encompassed chemical enterprises,
512 power plants, petrochemical industrial parks, and the Yangtze River in the YRD. This
513 evidence suggests that the region of southeast Yangzhou and lower reaches of the
514 Yangtze River are major source areas for the regionally transported BCc in Yangzhou
515 during lockdown.

516 Additionally, Luo et al. (2023) reported that regional transport of pollutants can occur
517 near the surface from upwind areas when the wind speed (WS) exceeds 2 m s⁻¹. **Figure**
518 **S5b** shows that the mean daytime WS was 3 m s⁻¹, indicating that both BC-fresh and
519 BC-aged particles, along with trace gases (e.g., SO₂, NO_x, and VOCs), originating from
520 the hotspot areas, could be transported effectively to Yangzhou. Additionally, the
521 average size of BCc remained around 600 nm at daytime (**Figure S5c**), suggesting that
522 BCc could undergo continual aging reactions under relatively lower RH, but produce
523 relatively thinly coated BCc with smaller sizes than those at nighttime (average size of
524 650 nm). The mean nocturnal WS decreased to 2 m s⁻¹, indicating that the regional
525 atmosphere becomes stagnant (**Figures S5a, b**). As mentioned earlier and underscored
526 here again, this stagnant and humid atmospheric condition may promote aqueous or
527 heterogeneous reactions, likely further leading to the production of more thickly coated
528 BCc than daytime ones.

529

530 **4. Conclusions and implications**

531 During the summer of 2021, the COVID-19 lockdown imposed in Yangzhou resulted
532 in a significant decrease in anthropogenic emissions from traffic and manufacturing
533 sectors. To examine the effects of this lockdown, we utilized spaceborne observations,
534 ground-based measurements, and particularly SPA-MS analysis to explore the
535 variations, aging characteristics, and sources of BCc in the YRD. We showed that the
536 strict emission controls effectively reduced local gaseous pollutants. However, the
537 decline in NO_x (~~-3039%~~) and TVOC (~~-514%~~) levels might on the other hand result in
538 increased O₃ (~~+19(28%)~~), leading to a rise in BC-aged particles and a slight elevation in
539 PM_{2.5} levels during the lockdown. Our results revealed a strong non-linear response of
540 PM_{2.5} and O₃ to the gaseous precursors.

541

542 The SPA-MS analysis results further demonstrate significant enhancement of OM and

设置了格式: 字体: Times New Roman

543 SNA coating species on BC-fresh particles, owing to gas-to-particle partitioning and
544 nocturnal multiphase chemistry. Consequently, we observed a higher fraction of BC-
545 aged particles (73%) during the lockdown due to enhanced oxidizing capacity and high
546 relative humidity (RH > 85%). The BC-fresh particles tended to mix with SNA under
547 high RH conditions, while high TVOC levels were accompanied by BCOC formation.
548 However, BCOC particles generally exhibited smaller sizes compared to BC-SNA
549 particles. Moreover, we propose that aqueous or heterogeneous reactions might be
550 important to generate BCOC and BC-SNA particles, especially ones with 400 nm D_{va} ,
551 while coagulation might play a more prominent role in larger BC-aged particles. The
552 aging process during LD promoted the conversion of partly coated particles to totally
553 coated ones, with larger diameters (600 nm) and thicker coatings.

554
555 It should be noted that the observed average $PM_{2.5}$ concentration during the lockdown
556 in Yangzhou was $24 \pm 20 \mu\text{g m}^{-3}$, which still significantly exceeds the WHO's air quality
557 guideline of $5 \mu\text{g m}^{-3}$. Our research underscores the crucial role of BCc, which
558 constitutes a significant portion of $PM_{2.5}$, in particulate matter pollution. These particles
559 originate from diverse combustion sources and their behavior is intricately influenced
560 by complex chemistry, regional transport, and meteorological factors. Mere reductions
561 in local primary emissions from traffic and manufacturing sectors exhibit limited
562 efficacy in air quality improvement. Therefore, effective air quality remediation
563 strategies necessitate nuanced control of BCc alongside broader emission reduction
564 efforts. We suggest a more comprehensive regulation of precursor gases from multiple
565 sectors, a wide-ranging joint regulation approach as well as proper consideration of the
566 chemistry, to develop an effective strategy for air quality improvement.

设置了格式: 非突出显示

567 **Data availability.** The data in this study are available from the corresponding author
568 upon request (caxinra@163.com).

569

570 **Author contributions.** XG, JW, and YD designed the research. YD, HW, and SC
571 conducted the field measurements. YD, HW, JW, and SC analyzed the data. XG, JW,
572 HL, YW, YZ, and EA reviewed the paper and provided useful suggestions. YD, JW,
573 and XG wrote the first draft of the paper. All people were involved in the discussion of
574 the results.

575

576 **Supplement.** The supplement related to this article is available online at XXX.

577

578 **Competing interests.** The contact author has declared that neither they nor their co-
579 authors have any competing interests.

580

581 **Financial support.** This research has been supported by the National Natural Science
582 Foundation of China (grant nos. 42377100, 22276099, and 42021004).

583 **References**

- 584 Adachi, K., Zaizen, Y., Kajino, M., Igarashi, Y., 2014. Mixing state of regionally
585 transported soot particles and the coating effect on their size and shape at a
586 mountain site in Japan. *Journal of Geophysical Research: Atmospheres* 119,
587 5386–5396. <https://doi.org/10.1002/2013JD020880>
- 588 Benedetti, A., Morcrette, J.-J., Boucher, O., Dethof, A., Engelen, R.J., Fisher, M.,
589 Flentje, H., Huneeus, N., Jones, L., Kaiser, J.W., Kinne, S., Mangold, A.,
590 Razinger, M., Simmons, A.J., Suttie, M., 2009. Aerosol analysis and forecast in
591 the European Centre for Medium-Range Weather Forecasts Integrated Forecast
592 System: 2. Data assimilation. *Journal of Geophysical Research: Atmospheres*
593 114. <https://doi.org/10.1029/2008JD011115>
- 594 Bond, T.C., Bergstrom, R.W., 2006. Light Absorption by Carbonaceous Particles: An
595 Investigative Review. *Aerosol Science and Technology* 40, 27–67.
596 <https://doi.org/10.1080/02786820500421521>
- 597 Bond, T.C., Doherty, S., Fahey, D.W., Forster, P., Berntsen, T., DeAngelo, B., Flanner,
598 M., Ghan, S., Kärcher, B., Koch, D., Kinne, S., Kondo, Y., Quinn, P.K., Sarofim,
599 M., Schultz, M., Michael, S., Venkataraman, C., Zhang, H., Zhang, S., Zender,
600 C.S., 2013. Bounding the role of black carbon in the climate system: A Scientific
601 assessment. *Journal of Geophysical Research: Atmospheres* 118, 5380–5552.
602 <https://doi.org/10.1002/jgrd.50171>
- 603 Cappa, C.D., Zhang, X., Russell, L.M., Collier, S., Lee, A.K.Y., Chen, C.-L., Betha, R.,
604 Chen, S., Liu, J., Price, D.J., Sanchez, K.J., McMeeking, G.R., Williams, L.R.,
605 Onasch, T.B., Worsnop, D.R., Abbatt, J., Zhang, Q., 2019. Light Absorption by
606 Ambient Black and Brown Carbon and its Dependence on Black Carbon
607 Coating State for Two California, USA, Cities in Winter and Summer. *Journal*
608 *of Geophysical Research: Atmospheres* 124, 1550–1577.
609 <https://doi.org/10.1029/2018JD029501>
- 610 Chang, Y., Huang, R., Ge, X., Huang, X., Hu, J., Duan, Y., Zou, Z., Liu, X., Lehmann,
611 M.F., 2020. Puzzling Haze Events in China During the Coronavirus (COVID-
612 19) Shutdown. *Geophys. Res. Lett.* 47. <https://doi.org/10.1029/2020GL088533>
- 613 Chen, H., Huo, J., Fu, Q., Duan, Y., Xiao, H., Chen, J., 2020. Impact of quarantine
614 measures on chemical compositions of PM_{2.5} during the COVID-19 epidemic
615 in Shanghai, China. *Science of The Total Environment* 743, 140758.
616 <https://doi.org/10.1016/j.scitotenv.2020.140758>
- 617 Chen, L., Qi, X., Nie, W., Wang, J., Xu, Zheng, Wang, T., Liu, Y., Shen, Y., Xu,
618 Zhengning, Kokkonen, T., Chi, X., Aalto, P., Paasonen, P., Kerminen, V.-M.,
619 Petäjä, T., Kulmala, M., Ding, A., 2021. Cluster Analysis of Submicron Particle
620 Number Size Distributions at the SORPES Station in the Yangtze River Delta
621 of East China. *Journal of Geophysical Research: Atmospheres* 126.
622 <https://doi.org/10.1029/2020JD034004>
- 623 Chen, L., Zhang, F., Yan, P., Wang, X., Sun, L., Li, Y., Zhang, X., Sun, Y., Li, Z., 2020.
624 The large proportion of black carbon (BC)-containing aerosols in the urban

625 atmosphere. *Environmental Pollution* 263, 114507.
626 <https://doi.org/10.1016/j.envpol.2020.114507>

627 Cheng, Y.F., Su, H., Rose, D., Gunthe, S.S., Berghof, M., Wehner, B., Achtert, P.,
628 Nowak, A., Takegawa, N., Kondo, Y., Shiraiwa, M., Gong, Y.G., Shao, M., Hu,
629 M., Zhu, T., Zhang, Y.H., Carmichael, G.R., Wiedensohler, A., Andreae, M.O.,
630 Pöschl, U., 2012. Size-resolved measurement of the mixing state of soot in the
631 megacity Beijing, China: diurnal cycle, aging and parameterization.
632 *Atmospheric Chemistry and Physics* 12, 4477–4491.
633 <https://doi.org/10.5194/acp-12-4477-2012>

634 Chien, L.-C., Chen, L.-W.A., Lin, R.-T., 2022. Lagged meteorological impacts on
635 COVID-19 incidence among high-risk counties in the United States—a
636 spatiotemporal analysis. *J Expo Sci Environ Epidemiol* 32, 774–781.
637 <https://doi.org/10.1038/s41370-021-00356-y>

638 Clemente, Á., Yubero, E., Nicolás, J.F., Caballero, S., Crespo, J., Galindo, N., 2022.
639 Changes in the concentration and composition of urban aerosols during the
640 COVID-19 lockdown. *Environmental Research* 203, 111788.
641 <https://doi.org/10.1016/j.envres.2021.111788>

642 Cui, S., Xian, J., Shen, F., Zhang, L., Deng, B., Zhang, Y., Ge, X., 2021. One-Year Real-
643 Time Measurement of Black Carbon in the Rural Area of Qingdao, Northeastern
644 China: Seasonal Variations, Meteorological Effects, and the COVID-19 Case
645 Analysis. *Atmosphere* 12, 394. <https://doi.org/10.3390/atmos12030394>

646 Cui, Y., Ji, D., Maenhaut, W., Gao, W., Zhang, R., Wang, Y., 2020. Levels and sources
647 of hourly PM_{2.5}-related elements during the control period of the COVID-19
648 pandemic at a rural site between Beijing and Tianjin. *Science of The Total
649 Environment* 744, 140840. <https://doi.org/10.1016/j.scitotenv.2020.140840>

650 Ding, A., Huang, X., Nie, W., Chi, X., Xu, Zheng, Zheng, L., Xu, Zhengning, Xie, Y.,
651 Qi, X., Shen, Y., Sun, P., Wang, J., Wang, L., Sun, J., Yang, X.-Q., Qin, W.,
652 Zhang, X., Cheng, W., Liu, W., Pan, L., Fu, C., 2019. Significant reduction of
653 PM_{2.5} in eastern China due to regional-scale emission control: evidence from
654 SORPES in 2011–2018. *Atmospheric Chemistry and Physics* 19, 11791–11801.
655 <https://doi.org/10.5194/acp-19-11791-2019>

656 Ding, S., Liu, D., Hu, K., Zhao, D., Tian, P., Wang, F., Li, R., Chen, Y., He, H., Huang,
657 M., Ding, D., 2021. Optical and hygroscopic properties of black carbon
658 influenced by particle microphysics at the top of the anthropogenically polluted
659 boundary layer. *Atmospheric Chemistry & Physics* 21, 681–694.
660 <https://doi.org/10.5194/acp-21-681-2021>

661 Feng, Z., Zheng, F., Liu, Y., Fan, X., Yan, C., Zhang, Y., Daellenbach, K.R., Bianchi, F.,
662 Petäjä, T., Kulmala, M., Bao, X., 2022. Evolution of organic carbon during
663 COVID-19 lockdown period: Possible contribution of nocturnal chemistry. *Sci
664 Total Environ* 808, 152191. <https://doi.org/10.1016/j.scitotenv.2021.152191>

665 Ge, B., Xu, D., Wild, O., Yao, X., Wang, J., Chen, X., Qixin, T., Pan, X., Wang, Z.,
666 2020. Inter-annual variations of wet deposition in Beijing during 2014–2017:

667 implications of below-cloud scavenging of inorganic aerosols.
668 <https://doi.org/10.5194/acp-2020-1146>

669 Gorelick, N., Hancher, M., Dixon, M., Ilyushchenko, S., Thau, D., Moore, R., 2017.
670 Google Earth Engine: Planetary-scale geospatial analysis for everyone. *Remote*
671 *Sensing of Environment, Big Remotely Sensed Data: tools, applications and*
672 *experiences* 202, 18–27. <https://doi.org/10.1016/j.rse.2017.06.031>

673 He, C., Liou, K.-N., Takano, Y., Zhang, R., Levy Zamora, M., Yang, P., Li, Q., Leung,
674 L.R., 2015. Variation of the radiative properties during black carbon aging:
675 theoretical and experimental intercomparison. *Atmospheric Chemistry and*
676 *Physics* 15, 11967–11980. <https://doi.org/10.5194/acp-15-11967-2015>

677 Hopke, P.K., Gao, N., Cheng, M.-D., 1993. Combining chemical and meteorological
678 data to infer source areas of airborne pollutants. *Chemometrics and Intelligent*
679 *Laboratory Systems, Proceedings of the 5th Conference on Computer*
680 *Applications in Analytical Chemistry (COMPANA '92)* 19, 187–199.
681 [https://doi.org/10.1016/0169-7439\(93\)80103-O](https://doi.org/10.1016/0169-7439(93)80103-O)

682 Huang, X., Ding, A., Gao, J., Zheng, B., Zhou, D., Qi, X., Tang, R., Wang, J., Ren, C.,
683 Nie, W., Chi, X., Xu, Z., Chen, L., Li, Y., Che, F., Pang, N., Wang, H., Tong, D.,
684 Qin, W., Cheng, W., Liu, W., Fu, Q., Liu, B., Chai, F., Davis, S.J., Zhang, Q.,
685 He, K., 2021. Enhanced secondary pollution offset reduction of primary
686 emissions during COVID-19 lockdown in China. *Natl Sci Rev* 8, nwaal37.
687 <https://doi.org/10.1093/nsr/nwaal37>

688 Huang, X., Wang, Z., Ding, A., 2018. Impact of Aerosol-PBL Interaction on Haze
689 Pollution: Multiyear Observational Evidences in North China. *Geophysical*
690 *Research Letters* 45, 8596–8603. <https://doi.org/10.1029/2018GL079239>

691 Isokääntä, S., Kim, P., Mikkonen, S., Kühn, T., Kokkola, H., Yli-Juuti, T., Heikkinen,
692 L., Luoma, K., Petäjä, T., Kipling, Z., Partridge, D., Virtanen, A., 2022. The
693 effect of clouds and precipitation on the aerosol concentrations and composition
694 in a boreal forest environment. *Atmospheric Chemistry and Physics* 22, 11823–
695 11843. <https://doi.org/10.5194/acp-22-11823-2022>

696 Jacobson, M.Z., 2002. Analysis of aerosol interactions with numerical techniques for
697 solving coagulation, nucleation, condensation, dissolution, and reversible
698 chemistry among multiple size distributions. *Journal of Geophysical Research:*
699 *Atmospheres* 107, AAC 2-1-AAC 2-23. <https://doi.org/10.1029/2001JD002044>

700 Jain, C.D., Madhavan, B.L., Singh, V., Prasad, P., Sai Krishnaveni, A., Ravi Kiran, V.,
701 Venkat Ratnam, M., 2021. Phase-wise analysis of the COVID-19 lockdown
702 impact on aerosol, radiation and trace gases and associated chemistry in a
703 tropical rural environment. *Environmental Research* 194, 110665.
704 <https://doi.org/10.1016/j.envres.2020.110665>

705 Jeong, C.-H., Yousif, M., Evans, G.J., 2022. Impact of the COVID-19 lockdown on the
706 chemical composition and sources of urban PM_{2.5}. *Environmental Pollution*
707 292, 118417. <https://doi.org/10.1016/j.envpol.2021.118417>

708 Kahnert, M., 2010. On the Discrepancy between Modeled and Measured Mass

709 Absorption Cross Sections of Light Absorbing Carbon Aerosols. *Aerosol*
710 *Science and Technology* 44, 453–460.
711 <https://doi.org/10.1080/02786821003733834>

712 Kandler, K., Schneiders, K., Ebert, M., Hartmann, M., Weinbruch, S., Prass, M.,
713 Pöhlker, C., 2018. Composition and mixing state of atmospheric aerosols
714 determined by electron microscopy: method development and application to
715 aged Saharan dust deposition in the Caribbean boundary layer. *Atmospheric*
716 *Chemistry and Physics* 18, 13429–13455. [https://doi.org/10.5194/acp-18-](https://doi.org/10.5194/acp-18-13429-2018)
717 [13429-2018](https://doi.org/10.5194/acp-18-13429-2018)

718 Kondo, Y., Matsui, H., Moteki, N., Sahu, L., Takegawa, N., Kajino, M., Zhao, Y.,
719 Cubison, M.J., Jimenez, J.L., Vay, S., Diskin, G.S., Anderson, B., Wisthaler, A.,
720 Mikoviny, T., Fuelberg, H.E., Blake, D.R., Huey, G., Weinheimer, A.J., Knapp,
721 D.J., Brune, W.H., 2011. Emissions of black carbon, organic, and inorganic
722 aerosols from biomass burning in North America and Asia in 2008. *Journal of*
723 *Geophysical Research: Atmospheres* 116.
724 <https://doi.org/10.1029/2010JD015152>

725 Laughner, J.L., Neu, J.L., Schimel, D., Wennberg, P.O., Barsanti, K., Bowman, K.W.,
726 Chatterjee, A., Croes, B.E., Fitzmaurice, H.L., Henze, D.K., Kim, J., Kort, E.A.,
727 Liu, Z., Miyazaki, K., Turner, A.J., Anenberg, S., Avise, J., Cao, H., Crisp, D.,
728 de Gouw, J., Eldering, A., Fyfe, J.C., Goldberg, D.L., Gurney, K.R.,
729 Hasheminassab, S., Hopkins, F., Ivey, C.E., Jones, D.B.A., Liu, J., Lovenduski,
730 N.S., Martin, R.V., McKinley, G.A., Ott, L., Poulter, B., Ru, M., Sander, S.P.,
731 Swart, N., Yung, Y.L., Zeng, Z.-C., 2021. Societal shifts due to COVID-19
732 reveal large-scale complexities and feedbacks between atmospheric chemistry
733 and climate change. *Proc Natl Acad Sci U S A* 118, e2109481118.
734 <https://doi.org/10.1073/pnas.2109481118>

735 Le, T., Wang, Y., Liu, L., Yang, J., Yung, Y.L., Li, G., Seinfeld, J.H., 2020. Unexpected
736 air pollution with marked emission reductions during the COVID-19 outbreak
737 in China. *Science* 369, 702–706. <https://doi.org/10.1126/science.abb7431>

738 Li, J., Jiang, L., Chen, C., Liu, D., Du, S., Zhang, Y., Yang, Y., Tang, L., 2020.
739 Characteristics and Sources of Black Carbon Aerosol in a Mega-City in the
740 Western Yangtze River Delta, China. *Atmosphere* 11, 315.
741 <https://doi.org/10.3390/atmos11040315>

742 Li, K., Wang, X., Lu, X., Chen, H., Yang, X., 2022. Effects of Volatile Components on
743 Mixing State and Size Distribution of Individual Black Carbon Aerosols.
744 *Aerosol Air Qual. Res.* 22, 210400. <https://doi.org/10.4209/aaqr.210400>

745 Li, L., Huang, Z., Dong, J., Li, M., Gao, W., Nian, H., Fu, Z., Zhang, G., Bi, X., Cheng,
746 P., Zhou, Z., 2011. Real time bipolar time-of-flight mass spectrometer for
747 analyzing single aerosol particles. *International Journal of Mass Spectrometry*
748 303, 118–124. <https://doi.org/10.1016/j.ijms.2011.01.017>

749 Li, L., Li, Q., Huang, L., Wang, Q., Zhu, A., Xu, J., Liu, Ziyi, Li, H., Shi, L., Li, R.,
750 Azari, M., Wang, Y., Zhang, X., Liu, Zhiqiang, Zhu, Y., Zhang, K., Xue, S., Ooi,

751 M.C.G., Zhang, D., Chan, A., 2020. Air quality changes during the COVID-19
752 lockdown over the Yangtze River Delta Region: An insight into the impact of
753 human activity pattern changes on air pollution variation. *Science of The Total*
754 *Environment* 732, 139282. <https://doi.org/10.1016/j.scitotenv.2020.139282>

755 Liu, D., Joshi, R., Wang, J., Yu, C., Allan, J.D., Coe, H., Flynn, M.J., Xie, C., Lee, J.,
756 Squires, F., Kotthaus, S., Grimmond, S., Ge, X., Sun, Y., Fu, P., 2019.
757 Contrasting physical properties of black carbon in urban Beijing between winter
758 and summer. *Atmospheric Chemistry and Physics* 19, 6749–6769.
759 <https://doi.org/10.5194/acp-19-6749-2019>

760 Liu, Q., Jing, B., Peng, C., Tong, S., Wang, W., Ge, M., 2016. Hygroscopicity of
761 internally mixed multi-component aerosol particles of atmospheric relevance.
762 *Atmospheric Environment* 125, 69–77.
763 <https://doi.org/10.1016/j.atmosenv.2015.11.003>

764 Luo, J., Li, Z., Zhang, C., Zhang, Q., Zhang, Yongming, Zhang, Ying, Curci, G.,
765 Chakrabarty, R.K., 2022. Regional impacts of black carbon morphologies on
766 shortwave aerosol–radiation interactions: a comparative study between the US
767 and China. *Atmospheric Chemistry and Physics* 22, 7647–7666.
768 <https://doi.org/10.5194/acp-22-7647-2022>

769 Moffet, R.C., Rödel, T.C., Kelly, S.T., Yu, X.Y., Carroll, G.T., Fast, J., Zaveri, R.A.,
770 Laskin, A., Gilles, M.K., 2013. Spectro-microscopic measurements of
771 carbonaceous aerosol aging in Central California. *Atmospheric Chemistry and*
772 *Physics* 13, 10445–10459. <https://doi.org/10.5194/acp-13-10445-2013>

773 Morcrette, J.-J., Boucher, O., Jones, L., Salmond, D., Bechtold, P., Beljaars, A.,
774 Benedetti, A., Bonet, A., Kaiser, J.W., Razinger, M., Schulz, M., Serrar, S.,
775 Simmons, A.J., Sofiev, M., Suttie, M., Tompkins, A.M., Untch, A., 2009.
776 Aerosol analysis and forecast in the European Centre for Medium-Range
777 Weather Forecasts Integrated Forecast System: Forward modeling. *Journal of*
778 *Geophysical Research: Atmospheres* 114.
779 <https://doi.org/10.1029/2008JD011235>

780 Nie, D., Shen, F., Wang, J., Ma, X., Li, Z., Ge, P., Ou, Y., Jiang, Y., Chen, Meijuan,
781 Chen, Mindong, Wang, T., Ge, X., 2021. Changes of air quality and its
782 associated health and economic burden in 31 provincial capital cities in China
783 during COVID-19 pandemic. *Atmos Res* 249, 105328.
784 <https://doi.org/10.1016/j.atmosres.2020.105328>

785 Peng, J., Hu, M., Guo, S., Du, Z., Zheng, Jing, Shang, D., Levy Zamora, M., Zeng, L.,
786 Shao, M., Wu, Y.-S., Zheng, Jun, Wang, Y., Glen, C.R., Collins, D.R., Molina,
787 M.J., Zhang, R., 2016. Markedly enhanced absorption and direct radiative
788 forcing of black carbon under polluted urban environments. *Proceedings of the*
789 *National Academy of Sciences* 113, 4266–4271.
790 <https://doi.org/10.1073/pnas.1602310113>

791 Polissar, A.V., Hopke, P.K., Paatero, P., Kaufmann, Y.J., Hall, D.K., Bodhaine, B.A.,
792 Dutton, E.G., Harris, J.M., 1999. The aerosol at Barrow, Alaska: long-term

793 trends and source locations. *Atmospheric Environment* 33, 2441–2458.
794 [https://doi.org/10.1016/S1352-2310\(98\)00423-3](https://doi.org/10.1016/S1352-2310(98)00423-3)

795 Qin, M., Hu, A., Mao, J., Li, X., Sheng, L., Sun, J., Li, J., Wang, X., Zhang, Y., Hu, J.,
796 2021. PM_{2.5} and O₃ relationships affected by the atmospheric oxidizing
797 capacity in the Yangtze River Delta, China. *Science of The Total Environment*
798 152268. <https://doi.org/10.1016/j.scitotenv.2021.152268>

799 Ramanathan, V., Carmichael, G., 2008. Global and regional climate changes due to
800 black carbon. *Nature Geoscience* 1, 221–227. <https://doi.org/10.1038/ngeo156>

801 Sedlacek, A.J., Lewis, E.R., Onasch, T.B., Zuidema, P., Redemann, J., Jaffe, D.,
802 Kleinman, L.I., 2022. Using the Black Carbon Particle Mixing State to
803 Characterize the Lifecycle of Biomass Burning Aerosols. *Environ. Sci. Technol.*
804 56, 14315–14325. <https://doi.org/10.1021/acs.est.2c03851>

805 Silva, P.J., Liu, D.-Y., Noble, C.A., Prather, K.A., 1999. Size and Chemical
806 Characterization of Individual Particles Resulting from Biomass Burning of
807 Local Southern California Species. *Environ. Sci. Technol.* 33, 3068–3076.
808 <https://doi.org/10.1021/es980544p>

809 Song, X.-H., Hopke, P.K., Fergenson, D.P., Prather, K.A., 1999. Classification of Single
810 Particles Analyzed by ATOFMS Using an Artificial Neural Network, ART-2A.
811 *Anal. Chem.* 71, 860–865. <https://doi.org/10.1021/ac9809682>

812 Steinfeld, J.I., 1998. *Atmospheric Chemistry and Physics: From Air Pollution to*
813 *Climate Change. Environment: Science and Policy for Sustainable*
814 *Development* 40, 26–26. <https://doi.org/10.1080/00139157.1999.10544295>

815 Sulaymon, I.D., Zhang, Yuanxun, Hopke, P.K., Hu, J., Zhang, Yang, Li, L., Mei, X.,
816 Gong, K., Shi, Z., Zhao, B., Zhao, F., 2021a. Persistent high PM_{2.5} pollution
817 driven by unfavorable meteorological conditions during the COVID-19
818 lockdown period in the Beijing-Tianjin-Hebei region, China. *Environmental*
819 *Research* 198, 111186. <https://doi.org/10.1016/j.envres.2021.111186>

820 Sulaymon, I.D., Zhang, Yuanxun, Hopke, P.K., Zhang, Yang, Hua, J., Mei, X., 2021b.
821 COVID-19 pandemic in Wuhan: Ambient air quality and the relationships
822 between criteria air pollutants and meteorological variables before, during, and
823 after lockdown. *Atmospheric Research* 250, 105362.
824 <https://doi.org/10.1016/j.atmosres.2020.105362>

825 Sun, J., Sun, Y., Xie, C., Xu, Weiqi, Chen, C., Wang, Zhe, Li, L., Du, X., Huang, F., Li,
826 Y., Li, Z., Pan, X., Ma, N., Xu, Wanyun, Fu, P., Wang, Zifa, 2022. The chemical
827 composition and mixing state of BC-containing particles and the implications
828 on light absorption enhancement. *Atmos. Chem. Phys.* 22, 7619–7630.
829 <https://doi.org/10.5194/acp-22-7619-2022>

830 Sun, J., Wang, Zhe, Zhou, W., Xie, C., Wu, C., Chen, C., Han, T., Wang, Q., Li, Z., Li,
831 J., Fu, P., Wang, Zifa, Sun, Y., 2021. Measurement report: Long-term changes
832 in black carbon and aerosol optical properties from 2012 to 2020 in Beijing,
833 China (preprint). *Aerosols/Field Measurements/Troposphere/Physics (physical*
834 *properties and processes)*. <https://doi.org/10.5194/acp-2021-637>

- 835 Sun, Y., Du, W., Fu, P., Wang, Q., Li, J., Ge, X., Zhang, Q., Zhu, C., Ren, L., Xu, W.,
836 Zhao, J., Han, T., Worsnop, D.R., Wang, Z., 2016. Primary and secondary
837 aerosols in Beijing in winter: sources, variations and processes. *Atmos. Chem.*
838 *Phys.*
- 839 Sun, Y., Lei, L., Zhou, W., Chen, C., He, Y., Sun, J., Li, Z., Xu, W., Wang, Q., Ji, D., Fu,
840 P., Wang, Z., Worsnop, D.R., 2020. A chemical cocktail during the COVID-19
841 outbreak in Beijing, China: Insights from six-year aerosol particle composition
842 measurements during the Chinese New Year holiday. *Science of The Total*
843 *Environment* 742, 140739. <https://doi.org/10.1016/j.scitotenv.2020.140739>
- 844 Taylor, J.W., Allan, J.D., Allen, G., Coe, H., Williams, P.I., Flynn, M.J., Le Breton, M.,
845 Muller, J.B.A., Percival, C.J., Oram, D., Forster, G., Lee, J.D., Rickard, A.R.,
846 Parrington, M., Palmer, P.I., 2014. Size-dependent wet removal of black carbon
847 in Canadian biomass burning plumes. *Atmospheric Chemistry and Physics* 14,
848 13755–13771. <https://doi.org/10.5194/acp-14-13755-2014>
- 849 Wang, H., Miao, Q., Shen, L., Yang, Q., Wu, Y., Wei, H., 2021. Air pollutant variations
850 in Suzhou during the 2019 novel coronavirus (COVID-19) lockdown of 2020:
851 High time-resolution measurements of aerosol chemical compositions and
852 source apportionment. *Environmental Pollution* 271, 116298.
853 <https://doi.org/10.1016/j.envpol.2020.116298>
- 854 Wang, J., Ge, X., Sonya, C., Ye, J., Lei, Y., Chen, M., Zhang, Q., 2022. Influence of
855 regional emission controls on the chemical composition, sources, and size
856 distributions of submicron aerosols: Insights from the 2014 Nanjing Youth
857 Olympic Games. *Science of The Total Environment* 807, 150869.
858 <https://doi.org/10.1016/j.scitotenv.2021.150869>
- 859 Wang, J., Liu, D., Ge, X., Wu, Y., Shen, F., Chen, M., Zhao, J., Xie, C., Wang, Q., Xu,
860 W., Zhang, J., Hu, J., Allan, J., Joshi, R., Fu, P., Coe, H., Sun, Y., 2019.
861 Characterization of black carbon-containing fine particles in Beijing during
862 wintertime. *Atmos. Chem. Phys.* 19, 447–458. <https://doi.org/10.5194/acp-19-447-2019>
- 864 Wang, Pengfei, Chen, K., Zhu, S., Wang, Peng, Zhang, H., 2020. Severe air pollution
865 events not avoided by reduced anthropogenic activities during COVID-19
866 outbreak. *Resources, Conservation and Recycling* 158, 104814.
867 <https://doi.org/10.1016/j.resconrec.2020.104814>
- 868 Wang, Q., Liu, S., Zhou, Y., Cao, J., Han, Y., Ni, H., Zhang, N., Huang, R., 2015.
869 Characteristics of Black Carbon Aerosol during the Chinese Lunar Year and
870 Weekdays in Xi'an, China. *Atmosphere* 6, 195–208.
871 <https://doi.org/10.3390/atmos6020195>
- 872 Wang, S., Zhao, M., Xing, J., Wu, Y., Zhou, Y., Lei, Y., He, K., Fu, L., Hao, J., 2010.
873 Quantifying the Air Pollutants Emission Reduction during the 2008 Olympic
874 Games in Beijing. *Environ. Sci. Technol.* 44, 2490–2496.
875 <https://doi.org/10.1021/es9028167>
- 876 Wang, Y., Zhu, S., Ma, J., Shen, J., Wang, Pengfei, Wang, Peng, Zhang, H., 2021.

877 Enhanced atmospheric oxidation capacity and associated ozone increases
878 during COVID-19 lockdown in the Yangtze River Delta. *Science of The Total*
879 *Environment* 768, 144796. <https://doi.org/10.1016/j.scitotenv.2020.144796>

880 Wang, Y.Q., 2014. MeteoInfo: GIS software for meteorological data visualization and
881 analysis. *Meteorological Applications* 21, 360–368.
882 <https://doi.org/10.1002/met.1345>

883 Wang, Y.Q., Zhang, X.Y., Draxler, R.R., 2009. TrajStat: GIS-based software that uses
884 various trajectory statistical analysis methods to identify potential sources from
885 long-term air pollution measurement data. *Environmental Modelling &*
886 *Software* 24, 938–939. <https://doi.org/10.1016/j.envsoft.2009.01.004>

887 WHO global air quality guidelines: Particulate matter (PM_{2.5} and PM₁₀), ozone,
888 nitrogen dioxide, sulfur dioxide and carbon monoxide, 2021. , WHO Guidelines
889 Approved by the Guidelines Review Committee. World Health Organization,
890 Geneva.

891 Xie, C., He, Y., Lei, L., Zhou, W., Liu, J., Wang, Q., Xu, W., Qiu, Y., Zhao, J., Sun, J.,
892 Li, L., Li, M., Zhou, Z., Fu, P., Wang, Z., Sun, Y., 2020. Contrasting mixing
893 state of black carbon-containing particles in summer and winter in Beijing.
894 *Environmental Pollution* 263, 114455.
895 <https://doi.org/10.1016/j.envpol.2020.114455>

896 Xu, J., Ge, X., Zhang, X., Zhao, W., Zhang, R., Zhang, Y., 2020. COVID-19 Impact on
897 the Concentration and Composition of Submicron Particulate Matter in a
898 Typical City of Northwest China. *Geophysical Research Letters* 47,
899 e2020GL089035. <https://doi.org/10.1029/2020GL089035>

900 Yang, J., Ma, S., Gao, B., Li, X., Zhang, Y., Cai, J., Li, M., Yao, L., Huang, B., Zheng,
901 M., 2017. Single particle mass spectral signatures from vehicle exhaust particles
902 and the source apportionment of on-line PM_{2.5} by single particle aerosol mass
903 spectrometry. *Science of The Total Environment* 593–594, 310–318.
904 <https://doi.org/10.1016/j.scitotenv.2017.03.099>

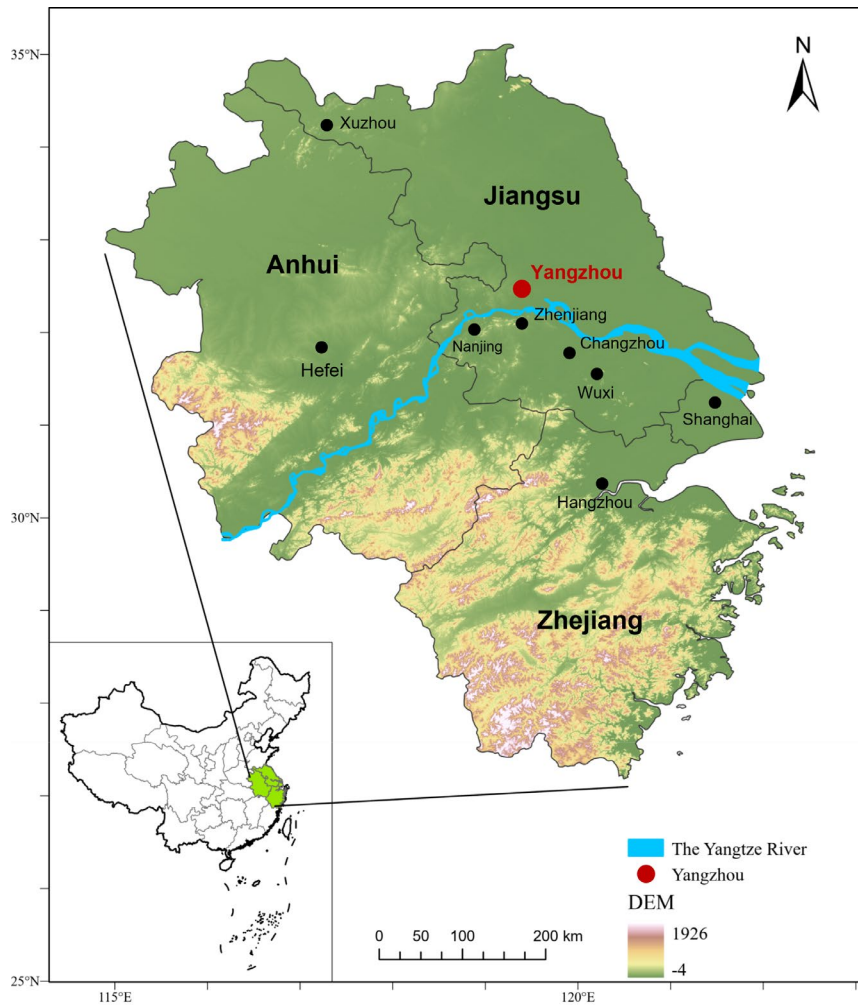
905 Zhang, G., Fu, Y., Peng, X., Sun, W., Shi, Z., Song, W., Hu, W., Chen, D., Lian, X., Li,
906 L., Tang, M., Wang, X., Bi, X., 2021. Black Carbon Involved Photochemistry
907 Enhances the Formation of Sulfate in the Ambient Atmosphere: Evidence From
908 In Situ Individual Particle Investigation. *Geophys Res Atmos* 126.
909 <https://doi.org/10.1029/2021JD035226>

910 Zhang, J., Li, H., Chen, L., Huang, X., Zhang, W., Zhao, R., 2022. Particle composition,
911 sources and evolution during the COVID-19 lockdown period in Chengdu,
912 southwest China: Insights from single particle aerosol mass spectrometer data.
913 *Atmospheric Environment* 268, 118844.
914 <https://doi.org/10.1016/j.atmosenv.2021.118844>

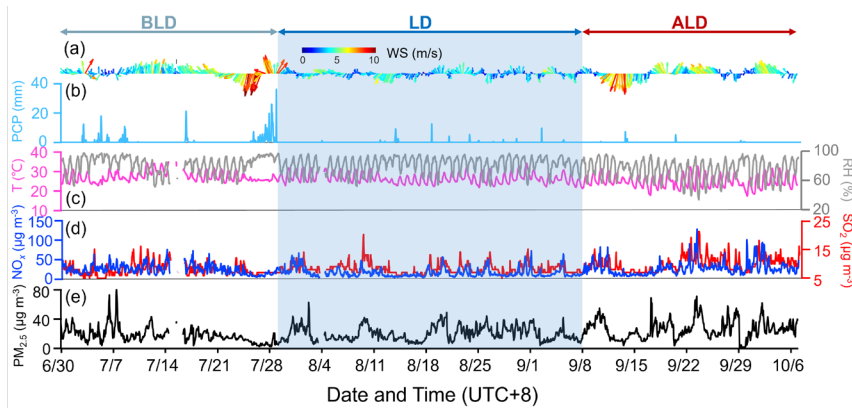
915 Zhang, J., Yuan, Q., Liu, L., Wang, Y., Zhang, Y., Xu, L., Pang, Y., Zhu, Y., Niu, H.,
916 Shao, L., Yang, S., Liu, H., Pan, X., Shi, Z., Hu, M., Fu, P., Li, W., 2021. Trans-
917 Regional Transport of Haze Particles From the North China Plain to Yangtze
918 River Delta During Winter. *JGR Atmospheres* 126.

919 <https://doi.org/10.1029/2020JD033778>
920 Zhang, K., Liu, Z., Zhang, X., Li, Q., Jensen, A., Tan, W., Huang, L., Wang, Y., de Gouw,
921 J., Li, L., 2022. Insights into the significant increase in ozone during COVID-
922 19 in a typical urban city of China. *Atmos. Chem. Phys.* 22, 4853–4866.
923 <https://doi.org/10.5194/acp-22-4853-2022>
924 Zhang, Y., Liu, X., Zhang, L., Tang, A., Goulding, K., Collett, J.L., 2021. Evolution of
925 secondary inorganic aerosols amidst improving PM2.5 air quality in the North
926 China plain. *Environmental Pollution* 281, 117027.
927 <https://doi.org/10.1016/j.envpol.2021.117027>
928 Zhang Y., Wang X., Chen H., Yang X., Chen J., Alien J.O., 2009. Source Apportionment
929 Of Lead-containing Aerosol Particles In Shanghai Using Single Particle Mass
930 Spectrometry. *Chemosphere* 74, 501–507.
931 Zhang, Y., Yuan, Q., Huang, D., Kong, S., Zhang, J., Wang, X., Lu, C., Shi, Z., Zhang,
932 X., Sun, Y., Wang, Z., Shao, L., Zhu, J., Li, W., 2018. Direct Observations of
933 Fine Primary Particles From Residential Coal Burning: Insights Into Their
934 Morphology, Composition, and Hygroscopicity. *Journal of Geophysical*
935 *Research: Atmospheres* 123, 12,964–12,979.
936 <https://doi.org/10.1029/2018JD028988>
937 Zhang, Z., Li, H., Ho, W., Cui, L., Men, Q., Cao, L., Zhang, Y., Wang, J., Huang, C.,
938 Lee, S., Huang, Y., Chen, M., Ge, X., 2024. Critical Roles of Surface-Enhanced
939 Heterogeneous Oxidation of SO₂ in Haze Chemistry: Review of Extended
940 Pathways for Complex Air Pollution. *Curr Pollution Rep.*
941 <https://doi.org/10.1007/s40726-023-00287-2>
942 Zhou, H., Liu, T., Sun, B., Tian, Y., Zhou, X., Hao, F., Chun, X., Wan, Z., Liu, P., Wang,
943 J., Du, D., 2022. Chemical characteristics and sources of PM2.5 in Hohhot, a
944 semi-arid city in northern China: insight from the COVID-19 lockdown. *Atmos.*
945 *Chem. Phys.* 14.
946 Zhou, X., Gao, J., Wang, T., Wu, W., Wang, W., 2009. Measurement of black carbon
947 aerosols near two Chinese megacities and the implications for improving
948 emission inventories. *Atmospheric Environment* 43, 3918–3924.
949 <https://doi.org/10.1016/j.atmosenv.2009.04.062>
950 Zhou, Y., Wu, Y., Yang, L., Fu, L., He, K., Wang, S., Hao, J., Chen, J., Li, C., 2010. The
951 impact of transportation control measures on emission reductions during the
952 2008 Olympic Games in Beijing, China. *Atmospheric Environment* 44, 285–
953 293. <https://doi.org/10.1016/j.atmosenv.2009.10.040>
954 Zhu, X., Hu, B., Xin, J., Wang, L., Munkel, C., Mao, G., Wang, Y., 2015. Impact of
955 emission controls on air quality in Beijing during APEC 2014: Lidar ceilometer
956 observations. *ATMOSPHERIC CHEMISTRY AND PHYSICS* 15, 12667–
957 12680. <https://doi.org/10.5194/acp-15-12667-2015>

958
959

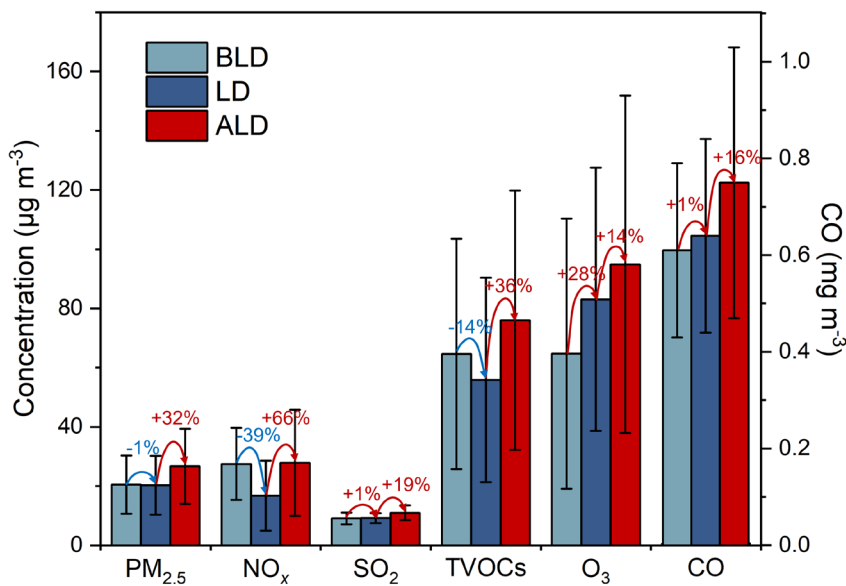


960
 961 Figure 1. Geographical overview of the Yangtze River Delta (YRD) Region in China,
 962 depicting the major cities within the YRD and the sampling site located in Yangzhou.
 963 The color gradient from green to white indicates varying altitudes across the region
 964 (Maps were generated by using ArcGIS Pro).



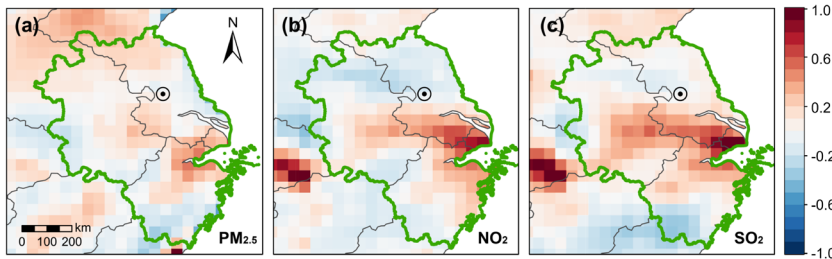
965

966 **Figure 2.** Temporal variations of (a) wind direction (WD) and wind speed (WS), (b)
 967 precipitation (PCP), (c) temperature (T) and relative humidity (RH), (d) concentrations
 968 of NO_x and SO_2 , and (e) mass loading of $\text{PM}_{2.5}$. The grey, blue, and red arrow ranges
 969 denote the periods before lockdown (BLD), during lockdown (LD), and after lockdown
 970 (ALD).



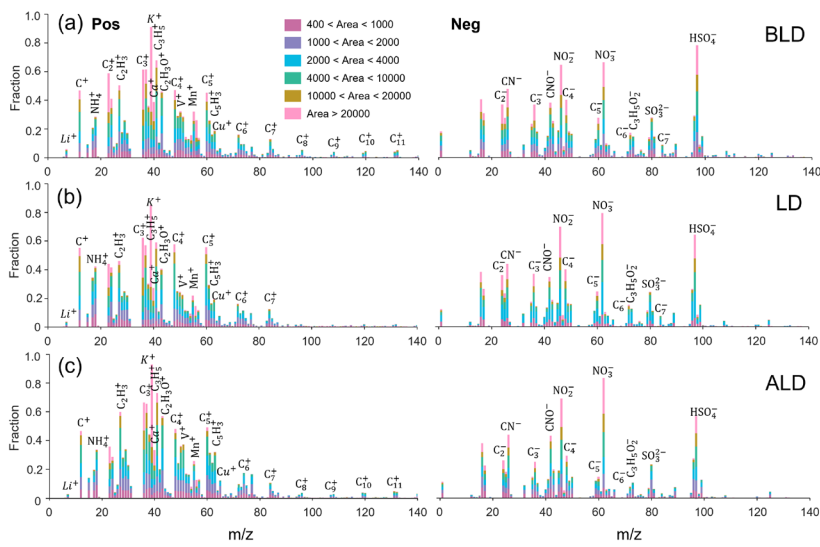
971

972 **Figure 3.** Ground-based observations of $\text{PM}_{2.5}$, NO_x , SO_2 , O_3 , CO , and TVOC
 973 concentrations in Yangzhou. The figure compares the averages during the BLD (grey),
 974 LD (blue), and ALD (red) periods. Error bars indicate SDs over different lockdown
 975 periods.
 976



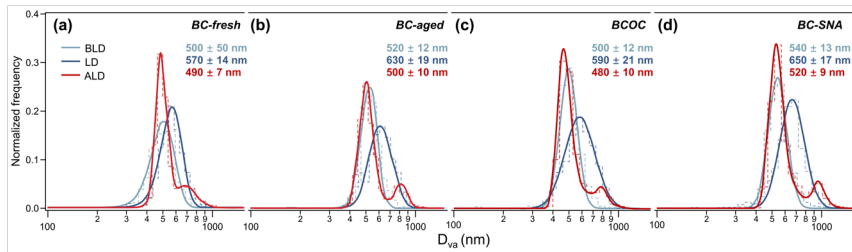
977
978
979
980
981

Figure 4. The fractional changes (i.e., $(LD - BLD)/BLD$) of (a) $PM_{2.5}$, (b) NO_2 , and (c) SO_2 between BLD and LD periods based on spaceborne measurement. The circle symbols in the maps indicate the location of Yangzhou, and the green region represents the YRD.



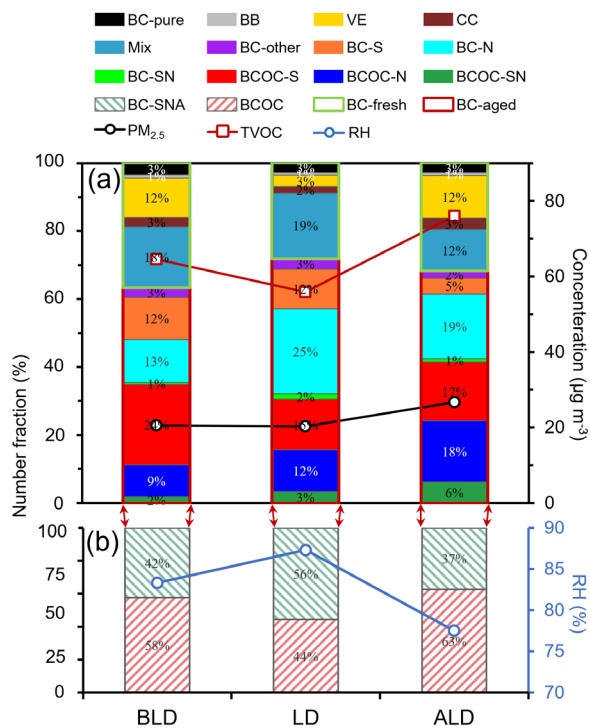
982
983
984
985
986

Figure 5. The average positive and negative mass spectra of BCc (a) before the lockdown period (BLD), (b) during the lockdown period (LD), and (c) after the lockdown period (ALD).



987
988
989
990
991
992
993

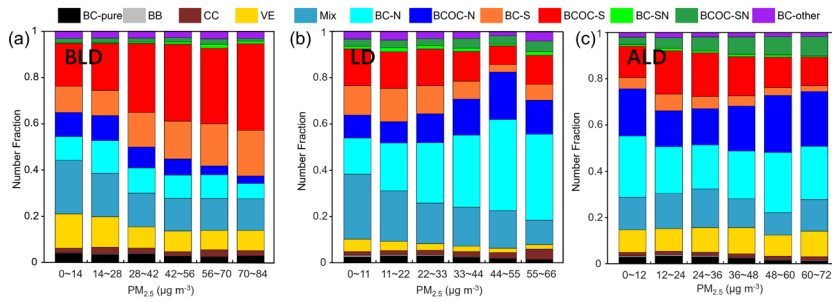
Figure 6. Size distribution of different types of BCc during different periods in Yangzhou. (a) BC-fresh particles, (b) BC-aged particles, (c) BCOC particles, and (d) BC-SNA particles. The Log-normal distribution was used to fit the unimodal size distribution, and the Lorentz distribution was used to fit the bimodal size distribution. The corresponding mode sizes (with the standard deviations) are also shown.



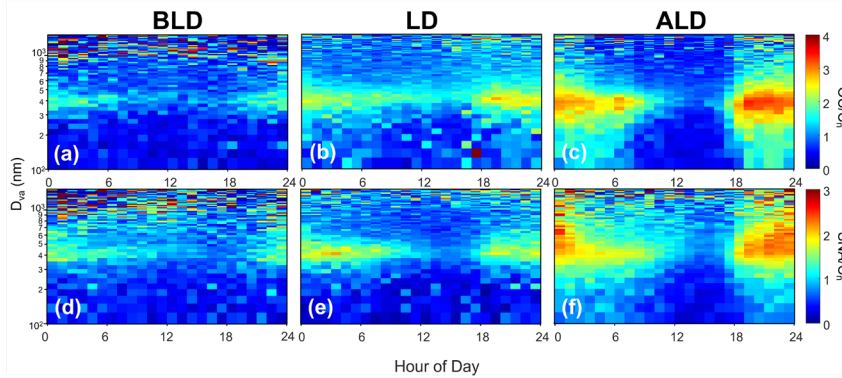
994
995

Figure 7. Number fractions of BCc. (a) The number fractions of different BCc along

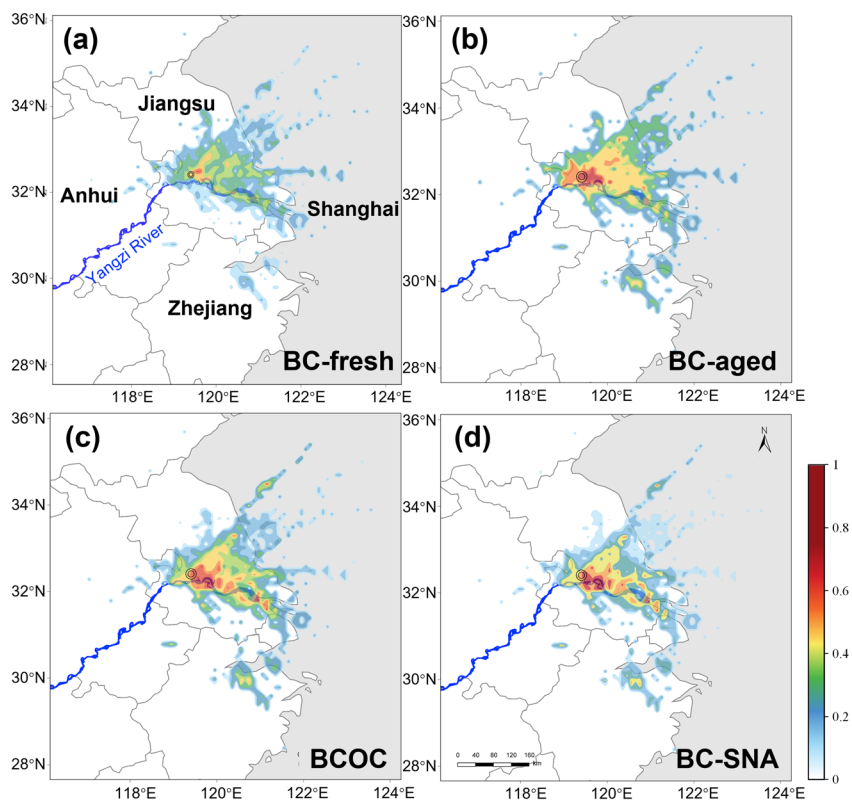
996 with the concentrations of $PM_{2.5}$ and total volatile organic compounds (TVOC). (b) The
 997 number fractions of different types of BC-aged particles along with relative humidity
 998 (RH).
 999



1000
 1001 **Figure 8.** Variations of number fractions of BCc particle types with $PM_{2.5}$ mass
 1002 concentrations during (a) the BLD period, (b) LD, and (c) the ALD period.



1003
 1004 **Figure 9.** Diurnal variations of the ratios of OC/Cn and SNA/Cn with a size distribution
 1005 of BCc during (a, d) BLD, (b, e) LD, and (c, f) ALD.



1006

1007 **Figure 10.** The PSCF maps for different BCc during LD. **(a)** BC-fresh. **(b)** BC-aged.
 1008 **(c)** BCOC. **(d)** BC-SNA.

1009

带格式的: 正文, 不允许文字在单词中间换行